

AE 2610, Lab #2

Analysis on Aerodynamic Loads

By: **Bryant Harrison**

Group A-09 X

Spring Semester 2025

Abstract

The effect of aerodynamic loads was experimentally evaluated on a rectangular, symmetrical wing with a removable end plate. Force and moment values were measured and then manipulated to compute the coefficients of lift, drag, and the pitching moment four times: twice with the wing's endplate, at ~16 m/s from an angle of attack of 0 to 22° and at ~12 m/s from an angle of attack of 0 to 20°, and twice without the wing's endplate, at ~16 m/s from an angle of attack of 0 to 22° and at ~12 m/s from an angle of attack of 0 to 20°. It was found that the higher speed produced more lift and less drag. Moreover, the end plate increased lift at a rate higher than it increased drag, also by benefiting flight efficiency by minimizing wing tip vortices. Furthermore, the wing was found to stall at 19.152°, 13.104°, 18.144°, and 12.096°, respectively, for the four scenarios tested. Thus, through this experiment, it is now known the safe operating angles of attack and that having the end plate and running at faster speeds produces the best flight conditions.

Introduction

Aerospace engineering is largely concerned with the impact of aerodynamic loads on structures. These aerodynamic loads can be summarized into three key loads: the lift force acting perpendicular to the direction of flight (often up), the drag force acting parallel to the direction of flight (often backwards), and the pitching moment serving to turn the structure up or down and increase its angle of attack – the angle between the main axis of the structure and the direction of flight. To see these loads on a small scale, this report details an airfoil (the cross section of a wing cut parallel to the direction of flight) under the effect of subsonic wind speed produced by a wind tunnel at differing angles of attack. The wing in question is a rectangular, symmetric wing. This wing has a removeable end plate that serves as a safeguard against wing tip vortices, an undesirable aerodynamic phenomenon. Thus, this experiment will investigate the loads with and without this end plate. Attached at the quarter-chord, the aerodynamic center of the airfoil – one-fourth of the length from the leading edge of the airfoil to its trailing edge, of this wing is a load cell that will measure the forces acting on the wing. The load cell has three cardinal directions and measures both the forces and moments acting on the load cell, and thus the wing, in the three respective directions at each stepped increase in the angle of attack. This setup will allow the investigation of the aerodynamic forces on the wing based on the presence of the end plate and the different speeds given by the subsonic wind tunnel.

Experimental Setup

First, the load cell is attached to the wing along its quarter-chord. The load cell will be used to measure the forces acting on the wing by the wind moving through the tunnel. The load cell is oriented with the y-axis pointing down the wind tunnel (towards the exit), the x-axis pointing clockwise from the wing's perspective (towards the operation room), and the z-axis then pointing

upwards (towards the ceiling). A diagram of this coordinate system can be found in the results and discussion section below. The wing is then mounted onto a stepper motor in the floor of the subsonic wind tunnel. This stepper motor is designed to turn the wing in one degree increments to simulate different angles of attack. The wind tunnel itself is a large tube with a super-sized fan at its entrance. There, air is drawn and accelerated to the desired velocity and then directed through a series of filters to reduce any turbulent motion. This air is further directed into a testing section, where the wing is placed. The wind tunnel can be operated at speeds up to approximately 35 m/s. During this experiment, it will be operated at the “high speed” of approximately 16 m/s and the “low speed” of approximately 12 m/s. Mounted to the wind tunnel is a pitot-static tube, with two holes. One is directed into the wind tunnel’s flow and the other is directed to the static air outside of the wind tunnel. These holes are then connected by long tubing to a Baratron. A pressure difference within the Baratron creates a change in capacitance that is then converted into an electrical signal and output as a voltage. This Baratron has an output voltage with a conversion factor of 1.016 millimeters of mercury per volt (mmHg/V) from voltage to pressure. Separated from the wind tunnel is the FlowKinetics Manometer, a device which measures the static (ambient) values of pressure, temperature, and density. Through the test, these values were measured to be a constant: $p_0 = 99.08 \text{ kPa}$, $T_0 = 21.1^\circ\text{C}$, $\rho_0 = 1.17304 \frac{\text{kg}}{\text{m}^3}$. The load cell’s and the Baratron’s data is sent to a facility-placed LabView VI, a computer that would compile the data for the loads and the Baratron voltage several hundred times a second at each indicated point controlled by the operator. This will be done at each degree of angle of attack four total times: *high speed with* the end plate, *low speed with* the end plate, *high speed without* the end plate, and finally *low speed without* the end plate.

Results and Discussion

Aerodynamic Loads

The experiment is then conducted, producing two raw data files containing several hundred instances of: forces in the x, y, and z directions, moments in the x, y, and z directions and Baratron voltages at each angle of attack. The first step is to convert these forces and moments into the aerodynamic loads discussed above. Figure 1 shows the forces and moments on the airfoil in both the load-cell reference frame and the aerodynamic frame.

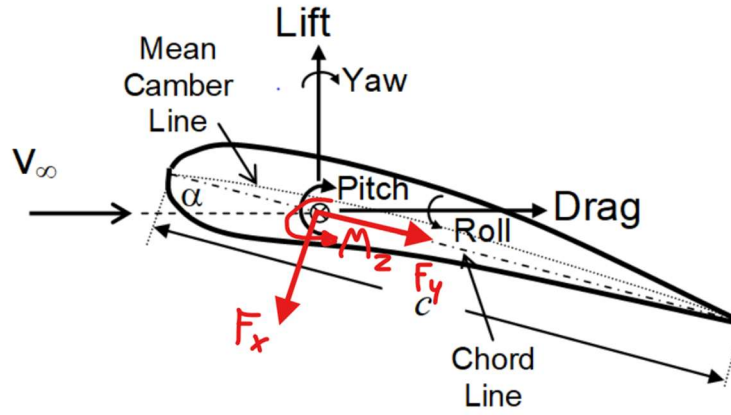


Figure 1. Aerodynamic forces on the symmetric, rectangular airfoil. Also depicted in red are the (resultants of) the forces in the x and y directions of the load cell as well as the moment in the z direction of the load cell. Image taken from lab manual.

These load cell values can then be converted into the aerodynamic forces by the following coordinate transformation (taking the lift-direction to be the new “x” -direction, the drag-direction to be the new “y” -direction and the pitch-direction to be the new “z” -direction):

$$L = -F_x \cos(\alpha) - F_y \sin(\alpha), \quad (1)$$

$$D = F_y \cos(\alpha) - F_x \sin(\alpha), \quad (2)$$

$$M = -M_z, \quad (3)$$

where L is the lift force, D is the drag force, M is the pitching moment, F_x is the force in the x-direction given by the load cell, F_y is the force in the y-direction given by the load cell, α is the angle of attack of the wing, and M_z is the moment in the z-direction given by the load cell.

Before analyzing the aerodynamic forces, it is important to realize that the data gathered is of a model of a wing that would be used in actual flight. Thus, it is beneficial to normalize these forces by the dynamic pressure and the wing's plan form area. The plan form area is given by the formula,

$$S = bc, \quad (4)$$

where b is the tip-to-tip length (span) of the wing and c is the chord length. The values of the span and the chord for this wing can be found in Table I.

Table I. Geometry of the wing used in this experiment.

Wing Geometry	Measurement (inches)
Chord	12.2
Span	27
Thickness Ratio	3

The dynamic pressure is the difference in the pressure within the wind tunnel and the stagnation pressure without the wind tunnel, called Bernoulli's equation:

$$q_\infty = p_0 - p, \quad (5)$$

where q_{∞} is the dynamic pressure, p_0 is the stagnation pressure, and p is the pressure of the flow. Since the pressure difference is recorded by the Baratron in terms of voltage, this relationship can instead be represented by a simple conversion:

$$q_{\infty} = XV, \quad (6)$$

where V is the voltage given by the Baratron and

$$X = \left(1.016 \frac{\text{mmHg}}{V}\right) \left(133.322 \frac{\text{Pascals}}{\text{mmHg}}\right) = 135.5 \frac{\text{Pa}}{V}$$

is the conversion factor from volts to dynamic pressure. With these two quantities defined, the aerodynamic loads can now be size- and speed-normalized.

First, lift can be normalized by the following formula:

$$C_L = \frac{L}{q_{\infty} S}, \quad (7)$$

where C_L is the normalized lift force, known as the coefficient of lift. Notice that the coefficient of lift is a dimensionless quantity and thus does not depend on the size of the wing or the pressure within the wind tunnel. Computing this coefficient for all four cases leads to the results found in Figure 2. As can be seen on the plot, the lift produced by higher speeds has the potential to be greater at larger angle of attacks. It appears as if higher speeds allow for sharper angles of attack, which in turn produce more lift than that of lesser angles of attack. During the experiment, it was noted that there was a sharp decrease in the lift forces at 19.152° , 13.104° , 18.144° , and 12.096° for the high speed with plate, low speed with plate, high speed without plate, and low speed without plate respectively. This phenomenon is displayed within Figure 2. In fact, this phenomenon is the act of stalling, where the wing has exceeded some threshold of the

angle of attack in which the wing is no longer able to produce significant lift. As one can tell from Figure 2, operating at higher speeds postpones stalling to greater angles of attack, a difference of about 5°. Moreover, the presence of the wing's end plate also postpones stalling by a less impactful but still significant 0-2°. Notice that there is error bars displayed on this figure. This shows the range of values that the coefficient of lift may take based on measurement and calculation errors. More on this is discussed in the appendix at the end of the report.

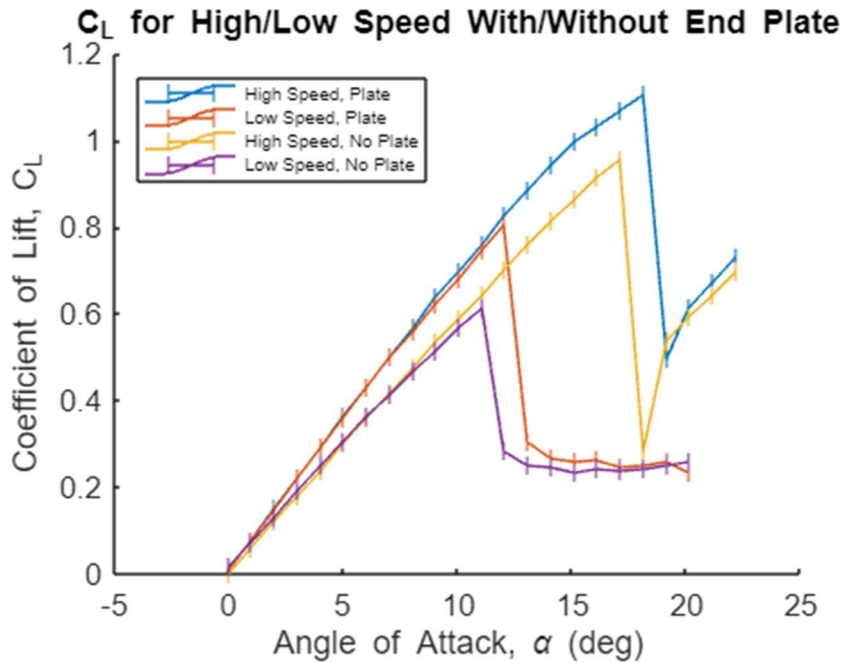


Figure 2. Coefficient of lift shown as a function (with error bars shown) of angle of attack for four cases: 16 m/s and 12 m/s for the wing with its end plate and 16 m/s and 12 m/s for the wing without its end plate.

Next, the drag force can be normalized by the following formula:

$$C_D = \frac{D}{q_\infty S} \quad (8)$$

where C_D is the normalized drag force, known as the coefficient of drag. Similar to the coefficient of lift, the coefficient of drag is also a dimensionless quantity. The coefficient of drag plotted against the angle of attack can be found in Figure 3. The most obvious trend is that the coefficient of drag increases with respect to the angle of attack. Also note that the same angles of stalling that saw a sharp decrease in the coefficient of lift are also present with the coefficient of drag, showing either a sharp increase or a spike in the drag curves. Another trend of note is that the end plate seemingly causes the wing to have increased drag, as at almost all angles of attack the high and low speed and plated wing coefficients have greater values than their counterparts on the wing without its plate. Akin to the coefficient of lift, error bars are shown to display the range of values of the coefficient of drag at each point.

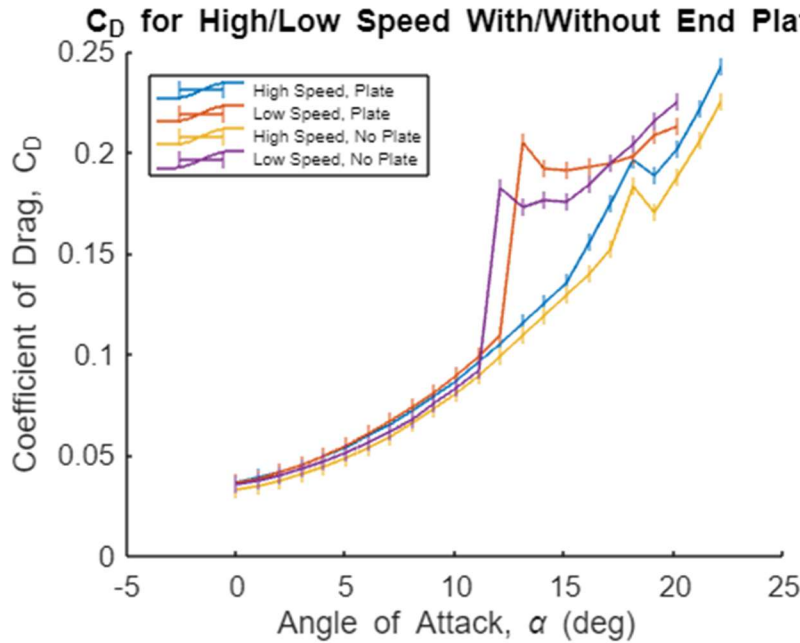


Figure 3. Coefficient of drag shown as a function (with error bars shown) of angle of attack for four cases: 16 m/s and 12 m/s for the wing with its end plate and 16 m/s and 12 m/s for the wing without its end plate.

Then, we can graph the coefficient of lift against the coefficient of drag, called the drag polar, instead of against the angles of attack. The drag polar will lead to new trends found within the data. Figure 4 shows the drag polar for the four scenarios studied. The most prevalent part of this graph is the big jumps that occur in each curve. These correspond to the coefficient values of stalling which resulted in a large decrease in the coefficient of lift and a large increase in the coefficient of drag, represented as straight lines demonstrating that decrease and increase. A key takeaway from a graph such as this is the slope of tangent lines at different parts of the plot. A slope at a particular point would reveal the ratio of lift to drag ($\frac{C_L}{C_D} = \frac{L}{D}$) at that point. The most desirable ratio is high, showing a large amount of lift with little drag. Typically, the slope of the drag polar is highest at low values of the drag coefficient. This corresponds to the lower angles of attack. As the curve begins to near the values that correspond to the stalling angle, the slope continually decreases. In particular, the high speed, plated wing curve becomes almost horizontal prior to stalling, representing an increase in drag without any counteracting increase in lift. One important thing of note is that the two curves with the end plate on the wing have greater slopes than the two curves without the end plate on the wing. This is important because it demonstrates that the wing with the end plate produces more lift than it does drag, as it was shown before that it increased both coefficients. Thus, the end plate is not hindering the flight of the wing, and it may benefit it. Error bars are also shown on this graph, but in two directions respectively indicating the range of the coefficient of drag and the coefficient of lift at each point.

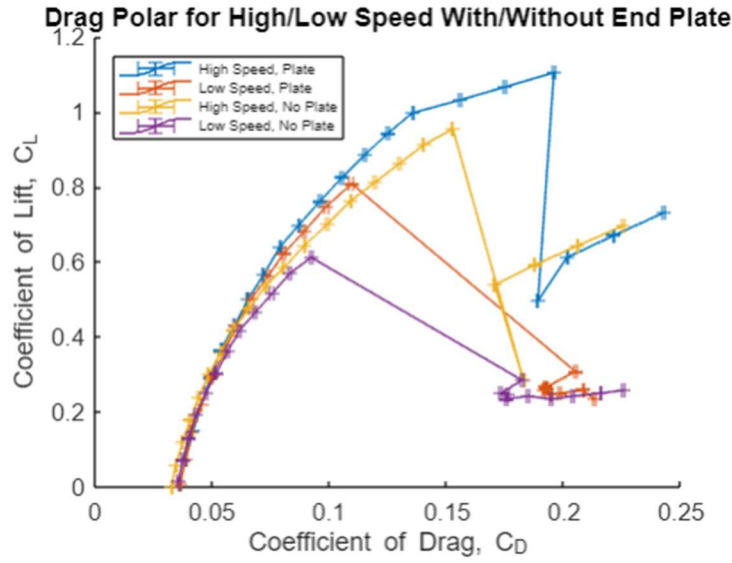


Figure 4. Coefficient of lift shown as a function (with error bars shown) of coefficient of drag for four cases: 16 m/s and 12 m/s for the wing with its end plate and 16 m/s and 12 m/s for the wing without its end plate.

Finally, the pitching moment can be normalized by the following formula:

$$C_M = \frac{M}{q_\infty S c}, \quad (9)$$

where C_M is the normalized pitch, called the coefficient of the pitching moment. Notice that Equation (9) differs from Equations (7) and (8) by the additional chord length in the denominator. This is because moments are a force times a distance, so an additional distance is needed to normalize a moment. The pitching moment coefficient can be plotted against the angle of attack just like the other two coefficients. This is done for all four scenarios in Figure 5. It is interesting to note that the pitching moment is zero when the angle of attack is also zero. This is because all forces on the wing act through the aerodynamic center, causing no moments to be produced about this center. However, as the angle of attack is increased, forces begin

to act at points other than the aerodynamic center, causing the coefficient to change in value. The pitching moment coefficient appears to steadily increase from zero by small amounts. Present in this graph also is the stalling angles of attack, in which the pitching moment coefficient greatly decreases. The behavior of the coefficient after this stall differs depending on the speed of the tunnel: at the high speeds, the pitching moment coefficient bounces back and begins to increase from just below the value when the stall begins; at the low speeds, the pitching moment coefficient remains at its decreased value and appears to oscillate around -0.05. It is unclear why this behavior occurs, but it is important to know of its presence so it can be accounted for if the angle of attack approaches the stalling values. Akin to the other coefficients, error bars are shown here, detailing the range of values the pitching moment coefficient can take on at each point.

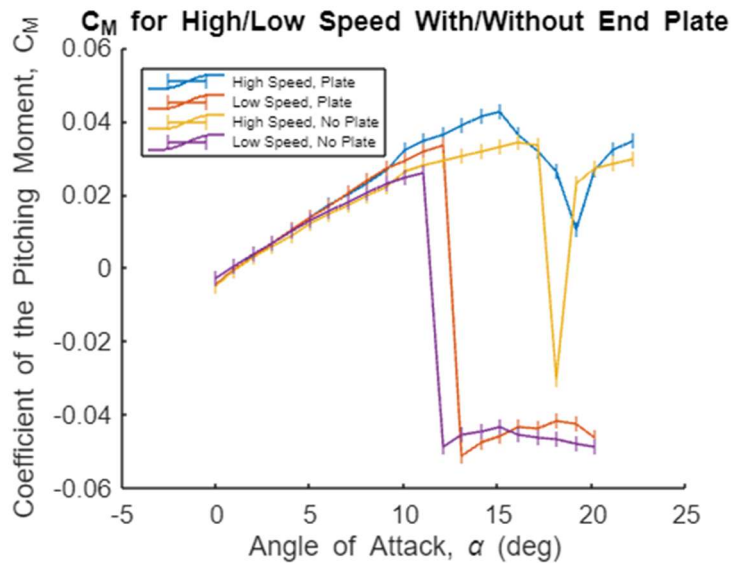


Figure 5. Coefficient of pitching moment shown as a function (with error bars shown) of angle of attack for four cases: 16 m/s and 12 m/s for the wing with its end plate and 16 m/s and 12 m/s for the wing without its end plate.

Additional Findings

Thin airfoil theory predicts that for a symmetric airfoil with an infinite span,

$$C_L = 2\pi\alpha. \quad (10)$$

Thus, for small to moderate angles of attack, the coefficient of lift should demonstrably be linearly proportional to the angle of attack by a factor of 2π . Applying a line of best fit for the linear sections of the coefficient of lift for the four scenarios yields the results in Figure 6. Note that the x-axis of Figure 6 is in radians, as opposed to the degrees used in previous figures. As one can see, the slopes of each of these lines is approximately $2\pi \approx 6.28$. This is the exact result expected by thin airfoil theory for the symmetric airfoil used in this experiment.

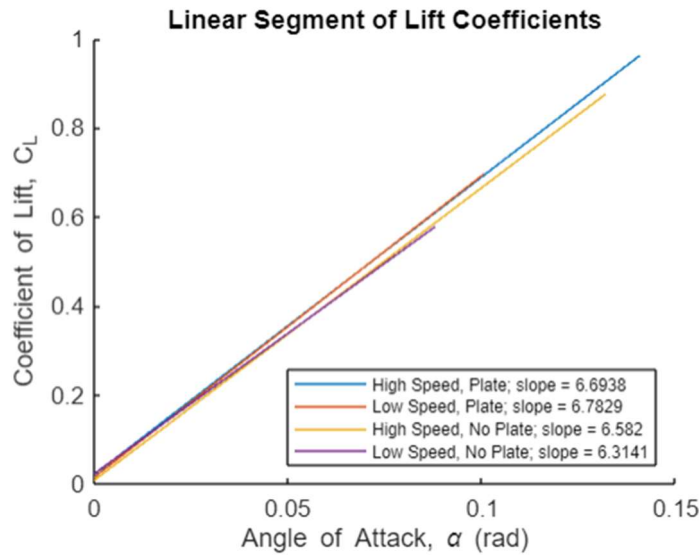


Figure 6. Lines of best fit for the linear section of the lift coefficients versus angles of attack for four cases: 16 m/s and 12 m/s for the wing with its end plate and 16 m/s and 12 m/s for the wing without its end plate.

To serve as a sanity check, the definition of dynamic pressure can be used to solve for the speed of the wind tunnel:

$$q_{\infty} = \frac{1}{2} \rho_{\infty} v_{\infty}^2. \quad (11)$$

Rearranging for the free-stream velocity and approximating that the free stream density is the stagnation density, it is found that:

$$v_{\infty} \approx \sqrt{2 \frac{q_{\infty}}{\rho_0}}. \quad (12)$$

Equation (12) can then be applied to each of the four scenarios to calculate the velocity of the wind in the wind tunnel. The results are that high speed with plate is 15.8926 m/s, low speed with plate is 12.5448 m/s, high speed without plate is 16.4081 m/s, and low speed without plate is 12.4557 m/s. These values are extremely close to 15.7 m/s, 12.4 m/s, 16.2 m/s, and 12.3 m/s respectively, recorded for each test. This means that the used calculation for the dynamic pressure is very close to its true value, with some variation likely due to the error in collecting the Baratron voltage (see the Appendix).

Summary and Conclusions

This report details the discussion of aerodynamic loads on a wing with a rectangular, symmetrical airfoil and with a removable end plate. This was done by attaching a load cell to the aerodynamic center of the wing and gathering data on the forces and moments acting on the wing at that point as wind is blown through a wind tunnel. The loads on the wing were then converted into the total lift force, drag force, and pitching moment. These new loads were then normalized by the size of the wing and turned into the coefficient of lift, coefficient of drag, and pitching moment coefficient, respectively. This process was conducted for four different cases within the wind tunnel: 16 m/s *with* the end plate, 12 m/s *with* the end plate, 16 m/s *without* the end plate, and

12 m/s *without* the end plate. The results showed that higher speeds produce more lift than lower speeds and that the wing with its end plate creates slightly more lift than that of the wing without its end plate. It was also shown that the coefficient of lift displayed the behavior of thin airfoil theory at small to moderate angles of attack, as it increased linearly with respect to the angle of attack. One of the most important findings is that the wing began to stall at 19.152° , 13.104° , 18.144° , and 12.096° angles of attack, respectively, for each of the four cases. Stalling is dangerous because it produces a sharp decrease in lift and a sharp increase in drag, often causing unsafe usage of an aircraft. Determining when a wing is about to stall is vital in the operation of that wing because it ensures the safety of operation at the specific angle of attack in question. Moreover, the plate causes the wing to have increased drag at almost all angles of attack. It is then important to consider if the increased lift from the plate is more than the increased drag, then showing whether the end plate is valid to use. From examining the drag polar of each case, it is clear that the coefficient of lift increase produced by the end plate is greater than the coefficient of drag increase produced by the end plate, as the slopes of the end plate-curves are greater than their corresponding no plate counterparts. This means that the end plate benefits the flight of the wing and does not hinder its ability to produce lift. Lastly, the pitching moment coefficient was found to be several magnitudes smaller than the other two coefficients. While not entirely negligible, these moments do not carry as much impact as the other forces. The behavior of the pitching moment coefficient at stalling was found to be dependent on the speed in the tunnel: low speeds created a drop and then an oscillation at some negative moment, while high speeds created a negative spike and an increase back to the previous value of the pitching moment. Thus, this experiment has allowed the determination of the effect of aerodynamic loads on a rectangular,

symmetrical airfoil at several subsonic conditions and evaluate when the wing runs at its most efficient and how to avoid dangerous areas of operation.

Appendix: Error Analysis

Loads

There are two sources of error that arise from the measurements in the loads: the precision and the bias uncertainties. The precision uncertainty, $u_{L,prec}$, is the randomness in the accuracy of the measurement of the loads. At each angle of attack, the loads are measured hundreds of times a second. Thus, there is a mean of these values and a standard deviation. With a 95% certainty in the measurements, we use the formula:

$$u_{i,prec} = 1.96 \frac{S_i}{\sqrt{N_i}}, \quad (\text{A.1})$$

where S_i is the standard deviation of the set of measurements and N_i is the number of values within the set of measurements. The systematic bias uncertainty is given by the manufacturer of the load cell as $u_{L,bias} = 0.05 \text{ N}$. Using these two uncertainty values, the total load uncertainty, u_L , can be calculated by:

$$u_i = \sqrt{u_{i,prec}^2 + u_{i,bias}^2} \quad (\text{A.2})$$

Applying Equations (A.1) and (A.2) to the load uncertainties will yield the total load uncertainty for each angle of attack. Then, note that:

$$u_{F_x} = u_L = u_{F_y}, \quad (\text{A.3})$$

where u_{F_x} and u_{F_y} are the total uncertainties in the force in the load cell's x-direction and the load cell's y-direction, respectively.

Moments

Equations (A.1) and (A.2) can similarly be applied to the moments measured by the load cell. The load cell manufacturer supplies the bias error in the load cell as $u_{M,bias} = 0.001 \text{ Nm}$. Similar to the load equations, note that:

$$u_{M_z} = u_M, \quad (\text{A.4})$$

where u_{M_z} is the total uncertainty in the moments in the z-direction of the load cell.

Baratron Voltage

Like the moment uncertainty, Equations (A.1) and (A.2) can be applied to the Baratron voltage as well. The Baratron manufacturer supplies the bias error as $u_{V,bias} = 0.002 \text{ V}$. Then, the total uncertainty in the Baratron voltage, u_V , can be found.

Coefficient of Lift

Now that the uncertainties in the raw measurements are known, the propagation of these uncertainties through the calculation of different quantities can be determined. First, the coefficient of lift will be evaluated. Plug Equations (1), (4), and (6) into Equation (7) to yield the coefficient of lift in terms of the raw measurements:

$$C_L = \frac{L}{q_\infty S} = \frac{-F_x \cos(\alpha) - F_y \sin(\alpha)}{XVbc}. \quad (\text{A.5})$$

Then, the uncertainty propagation equation can be applied:

$$u_y = \sqrt{\left(\frac{\partial y}{\partial x_1} u_{x_1}\right)^2 + \cdots + \left(\frac{\partial y}{\partial x_i} u_{x_i}\right)^2 + \cdots + \left(\frac{\partial y}{\partial x_n} u_{x_n}\right)^2}, \quad (\text{A.6})$$

where x_i are the raw measurements that y is dependent on and y is the variable in question. For the coefficient of lift, this looks like:

$$u_{C_L} = \sqrt{\left(\frac{\partial C_L}{\partial F_x} u_{F_x}\right)^2 + \left(\frac{\partial C_L}{\partial F_y} u_{F_y}\right)^2 + \left(\frac{\partial C_L}{\partial V} u_V\right)^2} \quad (\text{A.7})$$

Then, Equation (A.5) is used, and the partial derivatives are calculated to obtain the following:

$$\begin{aligned} u_{C_L} &= \sqrt{\left(\frac{-\cos(\alpha)}{XVbc} u_{F_x}\right)^2 + \left(\frac{-\sin(\alpha)}{XVbc} u_{F_y}\right)^2 + \left(\frac{F_x \cos(\alpha) + F_y \sin(\alpha)}{XV^2bc} u_V\right)^2} \\ &= \frac{1}{XVbc} \sqrt{(\cos(\alpha) u_{F_x})^2 + (\sin(\alpha) u_{F_y})^2 + \left(\frac{F_x \cos(\alpha) + F_y \sin(\alpha)}{V} u_V\right)^2}. \end{aligned}$$

Thus, the uncertainty in the coefficient of lift can be calculated at each angle of attack. This is the process that was used in the error bars in Figure 2 and the y-axis of Figure 4. The coefficient of lift has the most susceptibility to error, since its values are significantly larger than those of the other coefficients. The largest error in the coefficient of lift almost certainly arises from the uncertainties of the two forces, as those account for two of the three terms in the lift uncertainty. This uncertainty could be reduced by using a more precise load cell and reducing the bias uncertainty. Alternatively, even more samples of each measurement can be taken to lower the precision uncertainty (see Equation (A.1)) to near-zero.

Coefficient of Drag

This same process can be repeated for the coefficient of drag. Plugging Equations (2), (4), and (6) into Equation (8) yields:

$$C_D = \frac{D}{q_\infty S} = \frac{F_y \cos(\alpha) - F_x \sin(\alpha)}{XVbc}. \quad (\text{A.8})$$

Applying Equation (A.6) yields:

$$u_{C_D} = \sqrt{\left(\frac{\partial C_D}{\partial F_x} u_{F_x}\right)^2 + \left(\frac{\partial C_D}{\partial F_y} u_{F_y}\right)^2 + \left(\frac{\partial C_D}{\partial V} u_V\right)^2}, \quad (\text{A.9})$$

and then solving for the partial derivatives:

$$\begin{aligned} u_{C_D} &= \sqrt{\left(\frac{-\sin(\alpha)}{XVbc} u_{F_x}\right)^2 + \left(\frac{\cos(\alpha)}{XVbc} u_{F_y}\right)^2 + \left(\frac{F_x \sin(\alpha) - F_y \cos(\alpha)}{XV^2bc} u_V\right)^2} \\ &= \frac{1}{XVbc} \sqrt{(\sin(\alpha) u_{F_x})^2 + (\cos(\alpha) u_{F_y})^2 + \left(\frac{F_x \sin(\alpha) - F_y \cos(\alpha)}{V} u_V\right)^2}. \end{aligned}$$

This process was used for the calculation of the error bars in Figure 3 and the x-axis of Figure 4.

The largest source of error in the coefficient of drag is, like the coefficient of lift, likely to be the loads. This could be mitigated by the same ideas as above.

Coefficient of Pitching Moment

The same process can be repeated for the pitching moment coefficient. Plugging Equations (3), (4), and (6) into Equation (9) yields:

$$C_M = \frac{M}{q_\infty S c} = \frac{-M_z}{XVbc^2}. \quad (\text{A.10})$$

Applying Equation (A.6) yields:

$$u_{C_M} = \sqrt{\left(\frac{\partial C_M}{\partial M_z} u_{M_z}\right)^2 + \left(\frac{\partial C_M}{\partial V} u_V\right)^2}, \quad (\text{A.11})$$

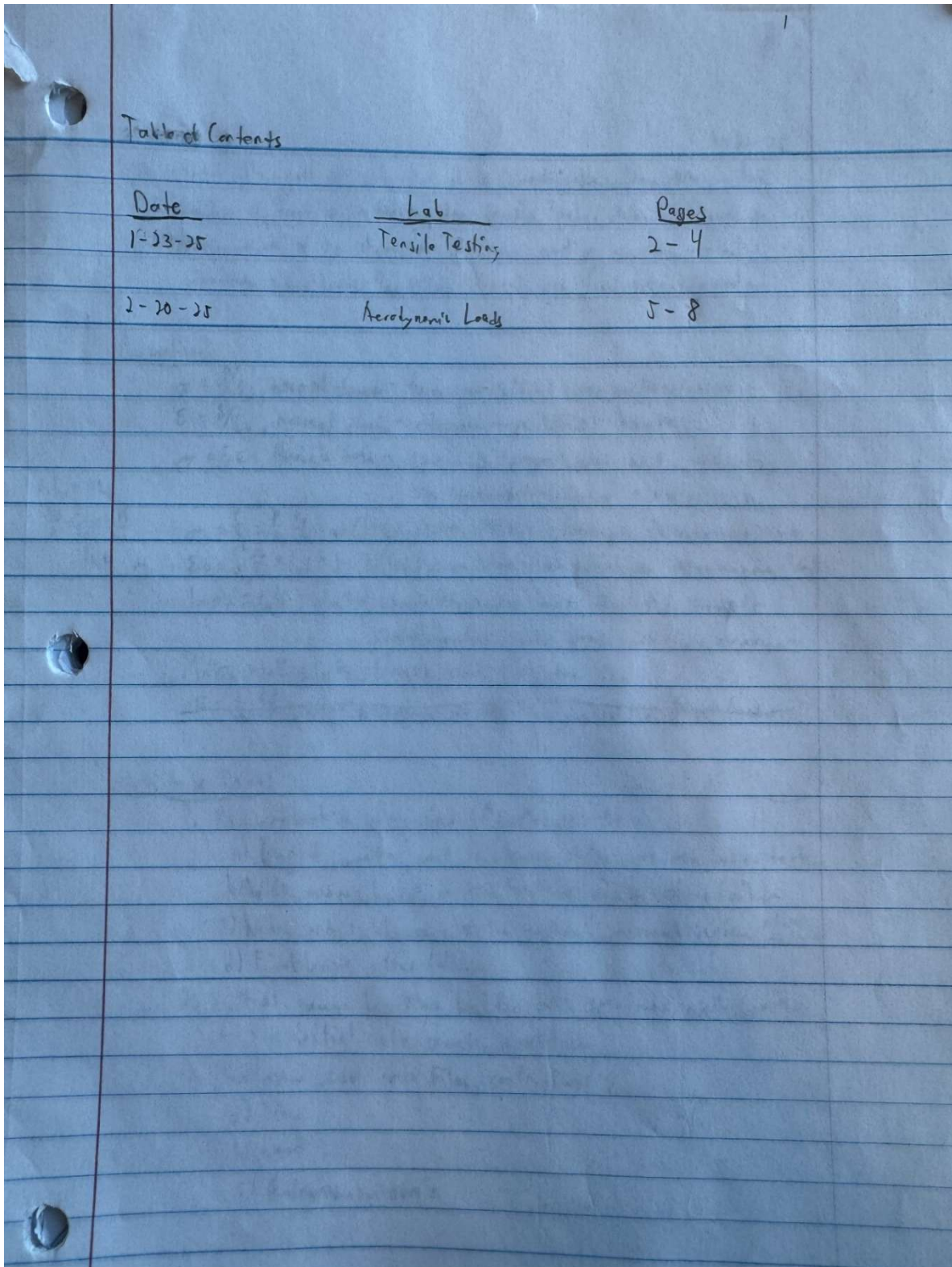
and then solving for the partial derivatives:

$$u_{C_M} = \sqrt{\left(\frac{-1}{XVbc^2} u_{M_z}\right)^2 + \left(\frac{M_z}{XV^2bc^2} u_V\right)^2}$$

$$= \frac{1}{XVbc^2} \sqrt{(u_{M_z})^2 + \left(\frac{M_z}{V} u_V\right)^2}.$$

This process was used in the calculation of the error bars in Figure 5. The largest source of error in the pitching moment coefficient is likely due in equal parts to the uncertainty in the moment in the z-direction of the load cell and the uncertainty in the Baratron voltage. The same principles of reducing this error from above still apply. However, one must also consider seeking a more accurate Baratron to reduce the bias uncertainty in the Baratron voltage.

Appendix: Lab Notebook



<u>Date</u>	<u>Lab</u>	<u>Pages</u>
1-23-25	Tensile Testing	2-4
2-20-25	Aerodynamic Loads	5-8

Figure A. Lab Notebook Page – Table of contents.

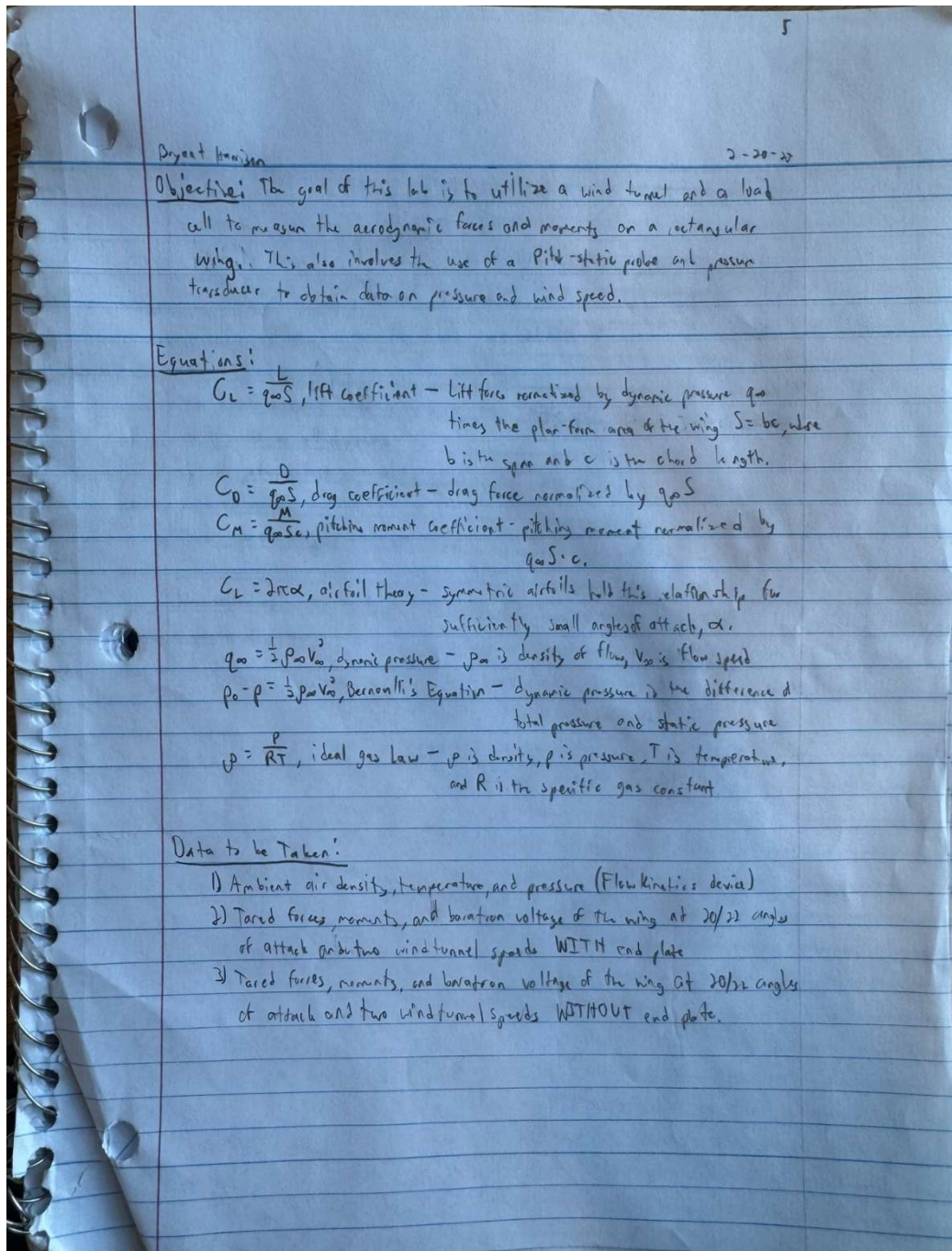


Figure B. Lab Notebook Page – Pre-lab information: objective, equations needed, and data to be collected.

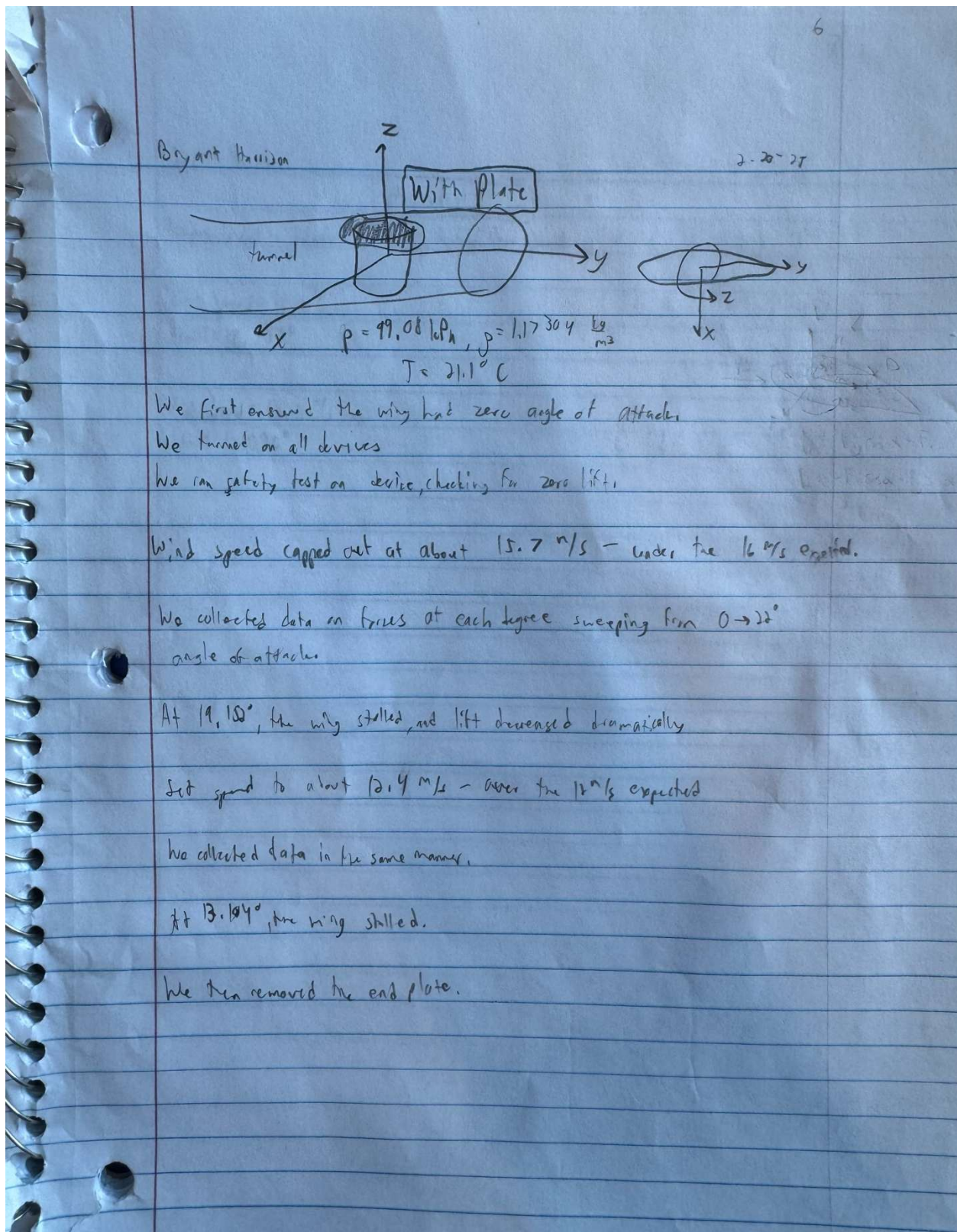


Figure C. Lab Notebook Page – Wing with end plate data and notes.

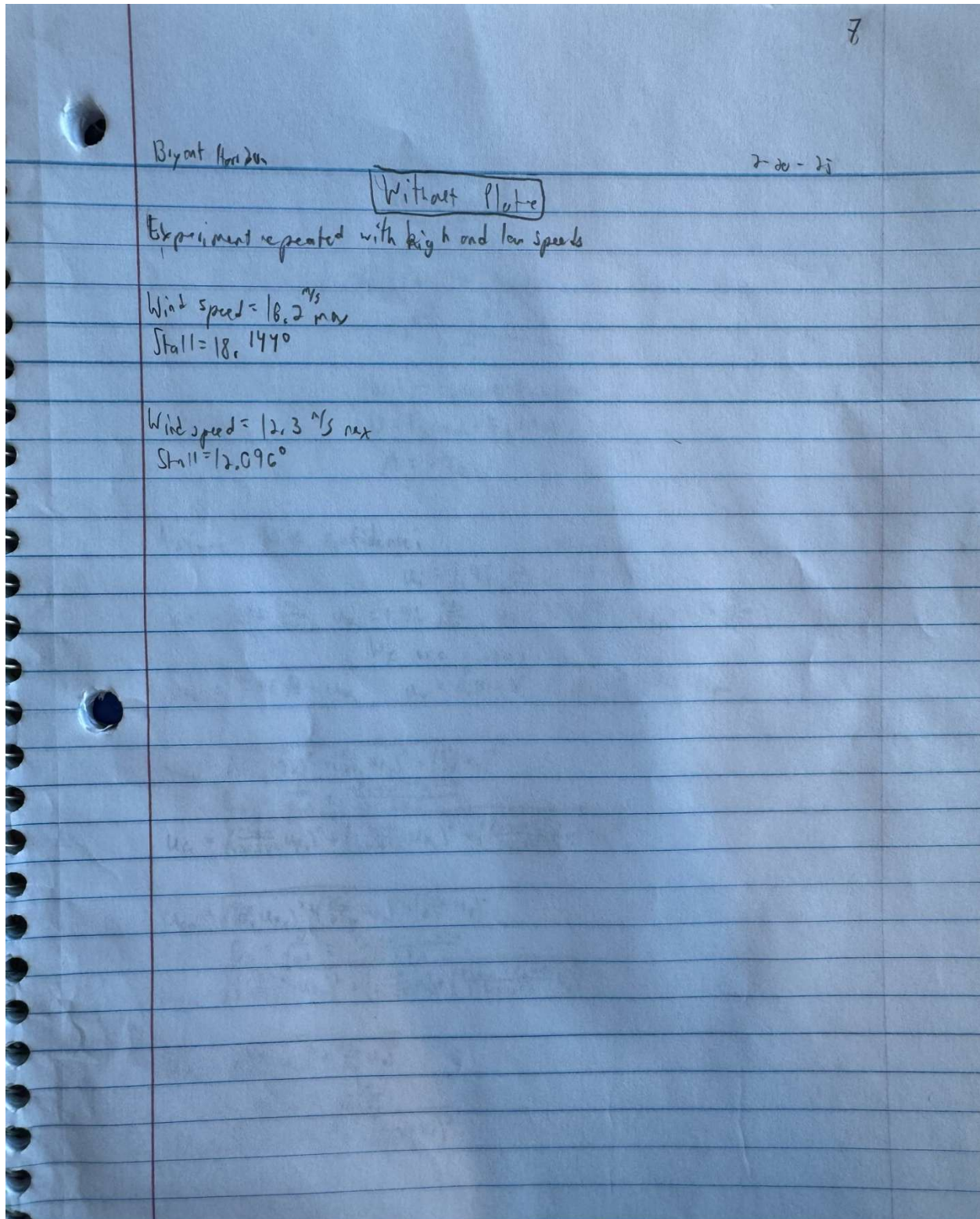


Figure D. Lab Notebook Page – Wing without end plate data and notes

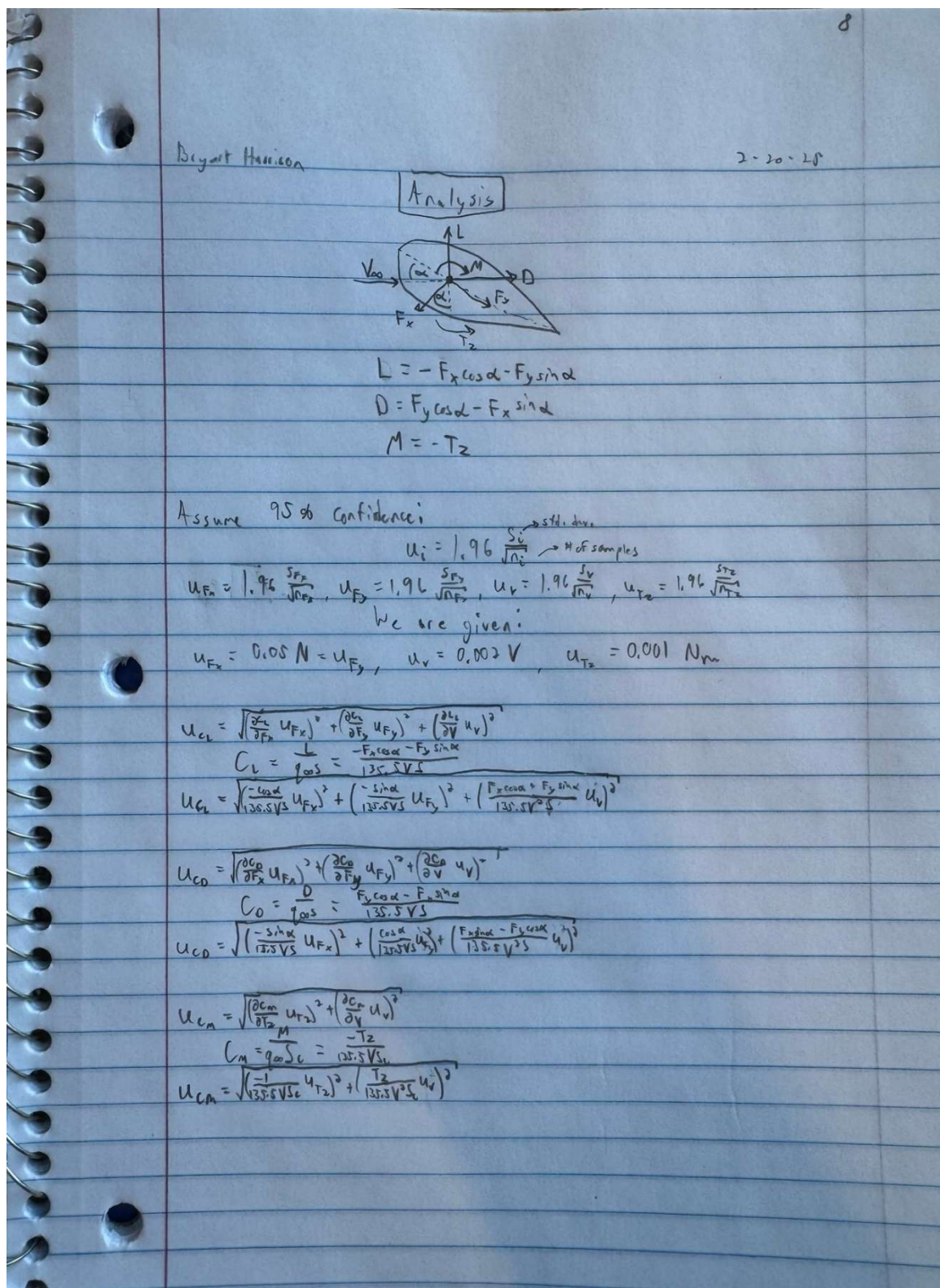


Figure E. Lab Notebook Page – Post-lab information: load, drag, pitching moment expressions and uncertainty expressions for further calculations.